Engineering Surface Oxygenated Functionalities on Commercial Carbon toward Ultrafast Sodium Storage in Ether-Based Electrolytes

Wei Xiao, Qian Sun, Jian Liu, Biwei Xiao, Xia Li, Per-Anders Glans, Jun Li, Ruying Li, Xifei Li, Jinghua Guo, Wanli Yang, Tsun-Kong Sham,* and Xueliang Sun*

ACCESS | Metrics & More | Article Recommendations | Supporting Information

ABSTRACT: The pursuit of a high-capacity anode material has been urgently required for commercializing sodium-ion batteries with a high energy density and an improved working safety. In the absence of thermodynamically stable sodium intercalated compounds with graphite, constructing nanostructures with expanded interlayer distances is still the mainstream option for developing high-performance carbonaceous anodes. In this regard, a surface-functionalized and pore-forming strategy through a facile CO_2 thermal etching route was rationally adopted to engineer negligible oxygenated functionalities on commercial carbon for boosting the sodium storage process. Benefitted from the abundant ionic/ electronic pathways and more active reaction sites in the microporous structure with noticeable pseudocapacitive behaviors, the functionalized porous carbon could achieve a highly reversible capacity of 505 mA h g^{-1} at 50 mA g^{-1}, an excellent rate performance of 181 mA h g^{-1} at 16,000 mA g^{-1}, and an exceptional rate cycle stability of 176 mA h g^{-1} at 3200 mA g^{-1} over 1000 cycles. These outstanding electrochemical properties should be ascribed to a synergistic mechanism, fully utilizing the graphitic and amorphous structures for synchronous intercalations of sodium ions and solvated sodium ion compounds, respectively. Additionally, the controllable generation and evolution of a robust but thin solid electrolyte interphase film with the emergence of obvious capacitive reactions on the defective surface, favoring the rapid migration of sodium ions and solvated species, also contribute to a remarkable electrochemical performance of this porous carbon black.

KEYWORDS: sodium-ion batteries, carbon anode, oxygenated functionalities, ether-based electrolyte, pseudocapacitive behavior
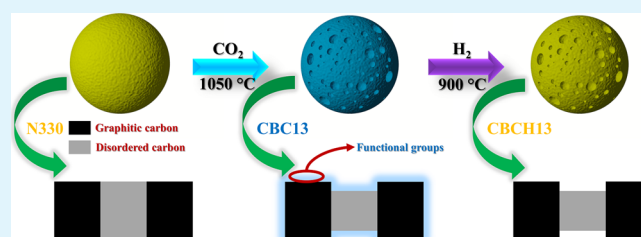
1. INTRODUCTION

Nowadays, the comprehensively technical penetration of lithium-ion batteries (LIBs) into portable devices has tremendously reshaped the modern consumer electronics and primarily propelled the development of electric vehicles and large-scale grid energy storage.[1−3] However, the haunting strategic anxiety concerning the gradual depletion of lithium resources and their geologically restrained distribution challenged the sustainability and affordability of LIBs in meeting the huge demands of electrical energy storage.[4,5] Sodium-ion batteries (SIBs), which inherit the analogous physicochemical properties of elemental sodium from the same group in the periodic table as lithium, have emerged as one of the most riveting alternatives for lithium counterparts for the ubiquitous sodium resources and subsequently low manufacturing cost.[6−10] The intrinsically disadvantageous energy density, resulting from a higher redox potential and a larger atomic weight as well as an increased ionic size, determined the huge potential of SIBs in applications of large-scale stationary and fluctuating energy storage for their cost-effectiveness.[5,8]

Particularly, the pursuit of advanced electrodes and electrolytes with high rate capabilities and cycle stabilities is the key to enable the high-performance SIBs for the sake of quick response to grid requirement.[11,12] However, the mismatch between a limited interlayer distance for a commercial graphite and a large ionic radius of sodium ion as well as the absence of a thermodynamically stable graphite intercalation compound[13,14] presented a serious challenge for the selection of a suitable anode substitute. Unfortunately, the sodium metal is severely plagued by safety issues regarding its low melting point and the unavoidable dendrite formation.[4] Initially, the disordered carbon materials, which are structurally composed of the curved graphene layers with large interlayer spacings and the turbostratic nanodomains with desirable pores, could generate reversible capacities as high as 300 mA h g^{-1}, but with relatively poor rate capabilities and cycle performances.[15−17] Inspired by lithium equivalents, the rational nanostructured design[18−26] and appropriate heteroatom doping[23,27−32] were widely employed to develop carbonaceous materials with a
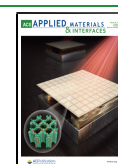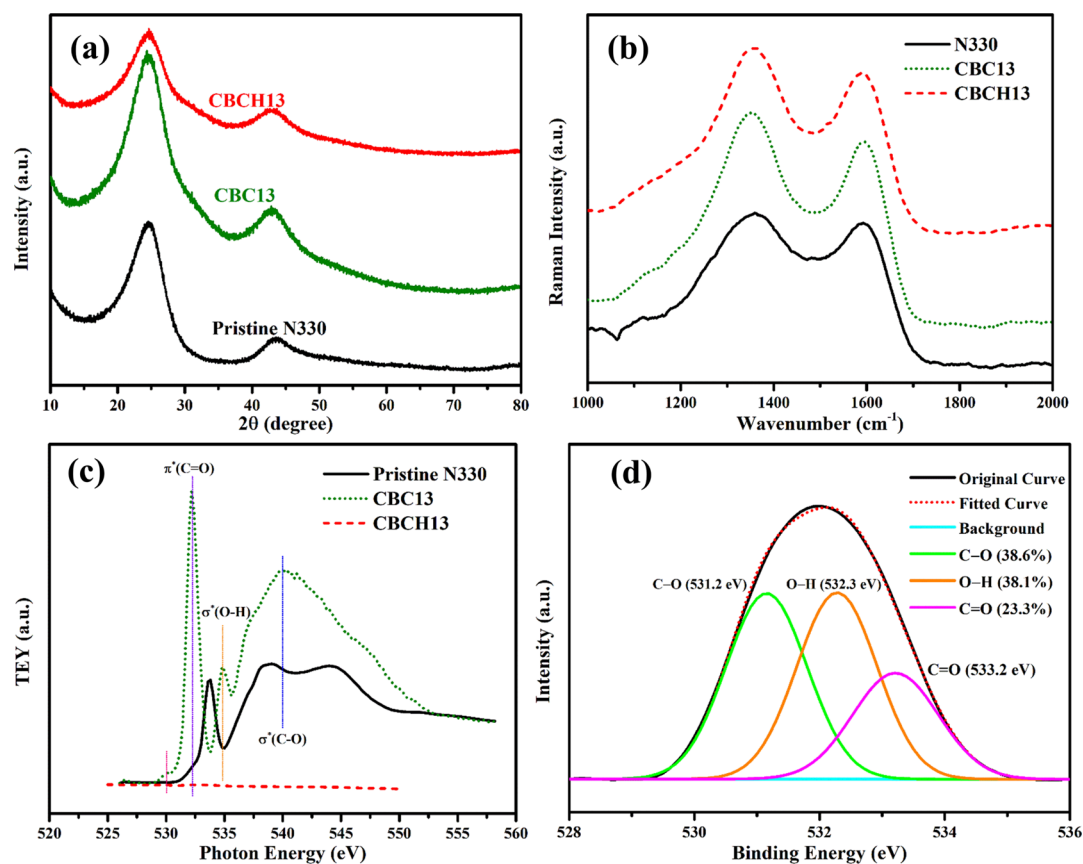
Figure 1. (a) XRD patterns, (b) Raman spectra, and (c) O K-edge XAS for different carbon blacks. (d) Synchrotron-based O 1s XPS for CBC13 carbon black.

high specific capacity and a long cycle life. Simultaneously, the electrochemical performances of carbon-based materials were further promoted by electrolyte optimization.[33−35] Recently, the layer-structure graphite has been revisited by several groups.[36−38] Jache and Adelhelm[36] surprisingly revealed a unique cointercalation phenomenon of sodium ions and diglyme solvents into graphite by forming a stable ternary intercalation compound with a highly reversible capacity of 100 mA h g^{-1}. Later, Kang et al.[37] further extended this electrochemical behavior to ether-based electrolytes and systematically studied the effects of different solvents/salts on electrochemical properties of natural graphite. According to these findings for ether-based electrolytes, the concept of solvent cointercalation has been gradually established for sodium ion storage in graphite.[39−41] Concurrently, the highly porous carbon materials in ether-based electrolytes could also deliver a large reversible capacity and a long-term cycle life for the emergence of a uniform and compact solid electrolyte interphase (SEI) layer with an improved structural stability.[40]

In our previous reports, the ether-based electrolyte was found to enable the highly reversible sodiation/desodiation processes for a commercial N330 carbon by efficiently incorporating solvated sodium ion compound cointercalation into the graphitic region with sodium ion insertion into the disordered structure.[42] Additionally, the desirable microstructure with abundant active sodium storage sites resulting from a NH$_3$-assisted thermal etching treatment of pristine carbon black can also give rise to a large reversible capacity and an ultralong cycle life.[43] Generally, several critical physicochemical properties involving the interlayer spacing, the

porosity, the surface area, the heteroatom doping, and the intercalation behaviors as well as the SEI formation in different electrolytes would definitely affect the electrochemical performances of carbon-based anode materials for SIBs.[44]

Herein, we first developed a surface-functionalized and pore-forming strategy for commercial carbon via a facile CO$_2$-assisted thermal etching route. With the assistance of an ether-based electrolyte to make most of active sodium storage sites, the functional groups could greatly boost the migrations of sodium ions/solvated species, effectively guarantee the rapid capacitive reactions on the defective surface, and favorably promote the sodium intercalation/extraction processes, further leading to a superior reversible capacity, an exceptional rate capability, and an outstanding cyclability.

2. EXPERIMENTAL SECTION

2.1. Materials Synthesis. The commercial N330 carbon black (Sid Richardson Carbon Corporation, USA) was selected as the pristine material, and the introduction of CO$_2$ at 1050 °C could lead to the formation of pores and oxygen-containing functional groups for carbon blacks, as elaborated in our previous report.[45] In a typical preparation, 500 mg of pristine carbon black distributed in a fused silica boat was pyrolyzed in a fused silica reactor under CO$_2$ at 1050 °C until the desired mass losses were obtained. The as-etched samples with the mass loss of 13, 30, and 50 wt % were referred as CBC13, CBC30, and CBC50, respectively. To explore the effects of oxygenated functionalities on electrochemical properties of carbon blacks, the as-obtained carbon blacks were further thermally treated under H$_2$ at 950 °C to effectively remove these oxygen-containing functional groups. The corresponding samples reduced from as-etched samples with the mass loss of 13, 30, and 50%, were denoted as CBCH13, CBCH30, and CBCH50, respectively.

In the preparation of electrolytes, sodium triflate ($NaCF_3SO_3$, 98%, Sigma-Aldrich) and molecular sieves (4 Å, Sigma-Aldrich) were initially dried at 150 °C under vacuum for 2 days. The residual water in the commercial solvents was further removed by the as-dried molecular sieves. Finally, the electrolytes using different solvents were carefully obtained in an Ar-filled glovebox by dissolving 1.0 M sodium triflate ($NaCF_3SO_3$, 98%, Sigma-Aldrich) into diethylene glycol dimethyl ether (DEGDME, 98.9%, Sigma-Aldrich) and ethylene carbonate (EC, 99%, BASF)/diethyl carbonate (DEC, 99%, BASF) with 1:1 as the volume ratio, respectively.

2.2. Physical Characterizations. X-ray diffraction (XRD) spectroscopy using a Bruker D8 ADVANCE (Cu Kα source, 40 kV, 40 mA) spectrometer was employed to study the crystalline structures of carbon blacks. Raman scattering spectra were recorded by a HORIBA Scientific LabRAM HR Raman spectrometer system with a 532.4 nm laser. N_2 adsorption/desorption isotherm and pore size distribution were measured by a Folio Micromeritics Tristar II surface area analyzer. The morphologies of different materials were observed by a Hitachi S-4800 field emission scanning electron microscope operated at 5 keV. High-resolution transmission electron microscopy (HRTEM) and electron energy-loss spectroscopy (EELS) elemental mapping were conducted by a Gatan GIF-200 spectrometer. In terms of synchrotron-based X-ray characterizations, O K-edge and C K-edge X-ray absorption spectroscopies (XAS) for different samples were collected at Beamline 6.3.1.2 and 8.0.1.4 of Advanced Light Source in Lawrence Berkeley National Laboratory. The C 1s and O 1s X-ray photoemission spectroscopies (XPS) were performed at the high-resolution spherical grating monochromator beamline in Canadian Light Source (CLS). The excitation/pass energy for C 1s and O 1s XPS are 700/20 and 1500/20 eV, respectively.

2.3. Electrochemical Measurements. The electrochemical properties of different carbon blacks were evaluated by the typical 2032-type coin cells. For electrode preparation, the slurry, obtained by thoroughly mixing 80 wt % active carbon materials, 10 wt % acetylene blacks as the conductive agent, and 10 wt % poly(vinylidene difluoride) binder in a certain amount of N-methyl pyrrolidinone solvent, was then casted onto a copper foil as the current collector. After drying under vacuum at 80 °C for 12 h, the as-formed electrodes were punched into 1/2 in. pellets and further pressed under a certain pressure with a loading mass of around 0.8 mg cm^{-2}. The 2032-type coin cells, which were composed of a sodium foil as the anode, a counter electrode as the cathode, a polypropylene membrane (Celgard 2400) as the separator, and electrolytes using different solvents, were assembled in a glovebox under an Ar atmosphere with limited moisture and oxygen contents. The galvanotactic charge–discharge tests were performed in a potential range of 0.001–2.5 V (vs Na/Na$^+$) at various current densities under room temperature by an Arbin BT-2000 Battery Tester. The cyclic voltammetry (CV) measurements were conducted by a versatile multichannel Biologic VMP3 electrochemical station at 0.1 mV s^{-1}, while the electrochemical impedance spectra (EIS) were collected at an AC (alternating current) voltage of 5 mV amplitude in the frequency range of 100 kHz to 0.01 Hz.

3. RESULTS AND DISCUSSION

The structural evolutions of different carbon blacks before and after the thermal treatments were studied by XRD and Raman spectra. XRD patterns in Figure 1a show two obvious peaks at ~24 and ~42°, corresponding to the (002) diffraction plane of layer-by-layer stacking structure for graphene and (100) diffraction plane of ordered hexagonal structure for graphite, respectively.[30,46] The coexistence of these two peaks further hints at an amorphous nature of different carbon blacks. According to the Bragg equation and Scherrer equation,[19,46] the interlayer distance (d_{002}), the in-lane coherence length (L_c), and the out-of-lane coherence length (L_a) for the graphitic domains are calculated and listed in Table S1 (Supporting Information). Even though the interlayer distance

(d_{002}) almost does not change after different thermal treatments, the value of L_c apparently increases while the value of L_a obviously decreases, indicating the reinforcement of short-range ordering structure and consumption of the amorphous part in pristine carbon black during the etching process, which agrees well with our previous results.[45] Furthermore, the introduction of CO_2 during the thermal treatment could markedly increase the surface area and create the pores with a smaller size. Meanwhile, the disordered (D) band induced from the defects in the disordered structure and the graphitic (G) band resulting from the graphitic structure in the crystallite can be identified at 1343 and 1590 cm^{-1} in Raman spectra, respectively.[46] As observed in Figure 1b, the peak for defect-induced D band obviously sharpens with the decrease in the related half width at half maximum upon CO_2 etching, while the peak for G band hardly changes, further confirming the decomposition of disordered part during the CO_2 thermal treatment. It is noteworthy that the strange increase in the I_D/I_G value after the CO_2 etching process at 1050 °C originated from the curling of stacked graphitic layers with the subsequent shrinkage of small graphitic crystals in (100) direction.[46,47] At the same time, the reduced carbon black after annealing in H_2 could present similar physical properties with a higher surface area and a larger pore size than that of the functionalized carbon black thermally treated in CO_2 (Figures S3 and S4). Importantly, the highly surface-sensitive O K-edge XAS in the total electron yield (TEY) mode were conducted to understand the surface functionalities and microstructures of different carbon blacks as shown in Figure 1c. For pristine N330 carbon black, a strong and broad peak at 533.7 eV can be assigned to the σ* state of C−O bond from the residual epoxide species, while two broad peaks at 538.5 and 544.0 eV should be ascribed to the σ* C−O transitions from the difference of two C−O bonds in carboxylic acids.[48−51] After the thermal etching in CO_2, CBC13 carbon black could display a weak feature at 530.0 eV and a sharp peak at 532.2 eV, undoubtedly arising from the transitions of O 1s electrons to the π* C=O states.[48,51] Additionally, an obvious peak at 534.9 eV and a broad peak at 540.0 eV should be derived from the σ* states of O−H and C−O bonds in hydroxyl groups, respectively.[49,50] When it comes to the carbon black after the thermal reduction in H_2, no signal can be observed. Concurrently, the full survey XPS for CBCH13 carbon black in Figure S10 also validates a complete elimination of oxygen feature upon H_2 thermal reduction of CBC13 carbon black. The evolution of chemical bonds, as evidenced in XAS measurements, clearly demonstrates the formation of functionalities in carbon black after the annealing process in CO_2 and the effective removal of oxygen-containing functional groups by the subsequent H_2 treatment. Furthermore, a high-resolution synchrotron-based O 1s XPS as depicted in Figure 1d was also applied to characterize the chemical states of oxygen in functionalized carbon. This broad peak could be deconvoluted accordingly into three peaks at 531.2, 532.3, and 533.2 eV, respectively. Two obvious peaks at 531.2 and 533.2 eV should be separately attributed to C−O and C=O bonds in the oxygenated functional groups, while the strong peak at 532.3 eV relates to the O−H bonds in functionalized carbon material.[52,53] Specifically, the proportions of C−O, O−H, and C=O bonds in oxygenated functional groups are estimated to be 38.6, 38.1, and 23.3%, respectively. At the same time, the corresponding peak in synchrotron-based C 1s XPS for CBC13 carbon black in
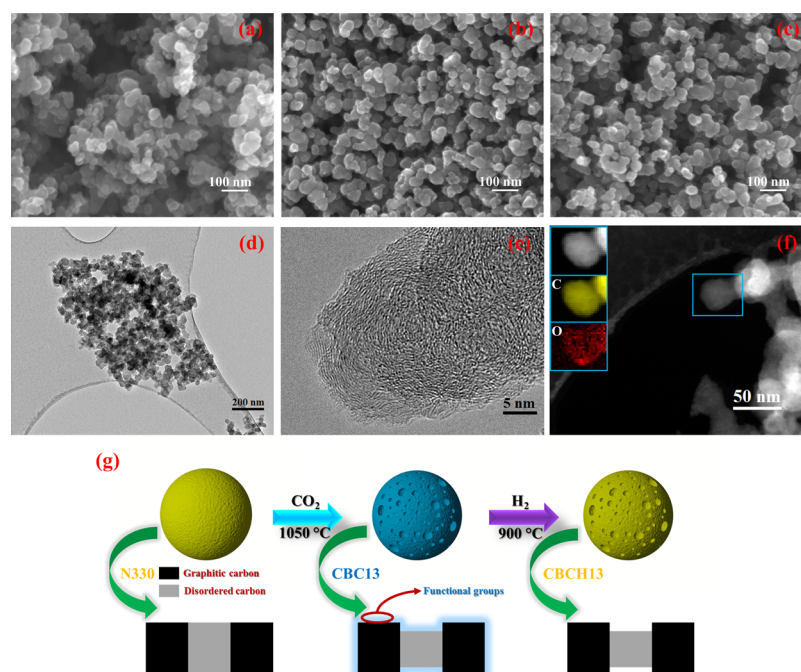
Figure 2. SEM images of (a) N330, (b) CBC13, and (c) CBCH13 carbon blacks. (d) TEM and (e) HRTEM images of CBC13 carbon black. (f) Elemental mappings in EELS for C and O K-edge of CBC13 carbon black. (g) Schematic diagram of the thermal etching and reducing processes.

Figure S2 can also be divided into C−C sp^2, C−C sp^3, C−O, and O=C−O peaks at 284.0, 285.2, 285.6, and 289.2 eV, respectively.[54−57] Moreover, the CO_2 thermal etching process would mildly increase the specific surface area from 78 m^2 g^{-1} for pristine N330 carbon black to 154 m^2 g^{-1} for CBC13 carbon black, while the average pore size was further reduced from 8.3 nm for pristine N330 carbon black to 5.3 nm for CBC13 carbon black, as shown in Table S1. Simultaneously, the pore volume and specific surface area for micropores would rise from 0.156 cm^3 g^{-1} and 10 m^2 g^{-1} for pristine N330 carbon black to 0.203 cm^3 g^{-1} and 95 m^2 g^{-1} for CBC13 carbon black, respectively. In addition, the tap density would decrease from 0.439 g cm^{-3} for pristine N330 carbon black to 0.414 g cm^{-3} for CBC13 carbon black after being thermally etched by CO_2. It is noteworthy that the H_2 thermal reduction process has barely changed these parameters for CBCH13 carbon black. Importantly, the rich and cogent information obtained from the underlying structural characterizations and exceptionally surface-sensitive detections, straightforwardly identified the decomposition of disordered part in the carbon structure and subsequent formation of microporosity as well as surface functionalities.

The morphologies and structures of different carbon blacks were further examined by SEM and TEM, as displayed in Figure 2a−f. In the pristine N330 carbon black, the irregular particles with the size ranging from 20 to 60 nm are unevenly distributed and severely aggregated. After the CO_2 thermal etching process, the tiny particles diminish, and the carbon black exhibits a granular morphology with a uniform particle size around 50 nm. Moreover, the H_2 thermal reduction could also slightly reduce the particle size without changing the spherical shape of carbon black. Compared with the pristine N330 carbon black, which tends to aggregate as microsized particles, the CBC13 carbon black derived from a CO_2 thermal etching treatment of N330 carbon black and CBCH13 carbon black obtained from a H_2 thermal reduction of CBC13 carbon

black would display a uniform distribution without noticeable agglomeration. Generally, the major particle aggregation for carbon nanomaterials relies on the electrostatic and van der Waals forces among various nanoparticles. After being thermally etched by CO_2 at 1050 °C, the as-obtained CBC13 carbon black is rich in negatively charged oxygenated functionalities (carboxyl, carbonyl, and hydroxyl), which would effectively relieve the electrostatic interactions among different carbon nanoparticles and suppress the potential particle agglomeration. Later, the thermal reduction of CBC13 carbon black by H_2 at 950 °C could efficiently remove all negative charges and electrostatic forces, leading to a homogeneous distribution of carbon nanoparticles. Specifically, an apparent short-range order in turbostatic nanodomains, as shown in the HRTEM image of Figure 2e, reveals an amorphous nature with a partially graphitic structure for CBC13 carbon black. Additionally, the elemental mappings in EELS at the C and O K-edge for Figures 2f and S1, critically confirm the intensive formation of oxygenated functionalities in the surface area of nanoparticles after the CO_2 thermal treatment. Figure 2g further illustrates the structural evolution of carbon black during the CO_2 thermal etching and H_2 thermal reducing processes. Upon reacting with CO_2 at 1050 °C, the disordered part would preferably decompose with the generation of oxygen-containing species on the surface of carbon black. Then, these oxygenated groups in the functionalized carbon black could be efficiently removed after the thermal reduction process in H_2 at 900 °C. The presence of oxygenated functionalities will unavoidably affect the reaction processes involving the sodium ion/solvated species migrations and subsequent electrochemical intercalation in carbon materials.

The pivotal roles of oxygenated functionalities can be proven by the dramatically different electrochemical performances, as evaluated by the galvanostatic discharge−charge measurements in an ether-based electrolyte for different carbon blacks. In Figure 3a, the CBC13 carbon black with abundant functional
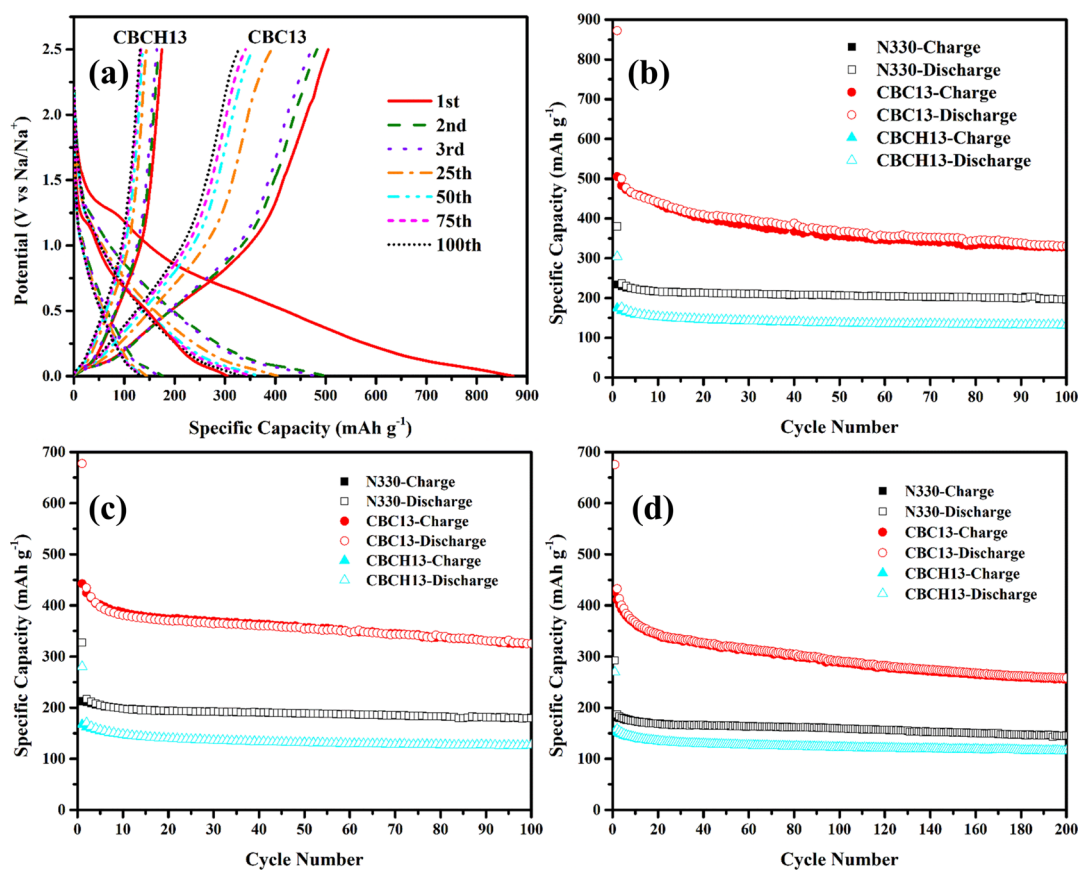
Figure 3. (a) Discharge−charge profiles for CBC13 and CBCH13 carbon black at a current density of 50 mA g^{-1}. Cycle performances of different carbon blacks at current densities of (b) 50, (c) 100, and (d) 200 mA g^{-1}.
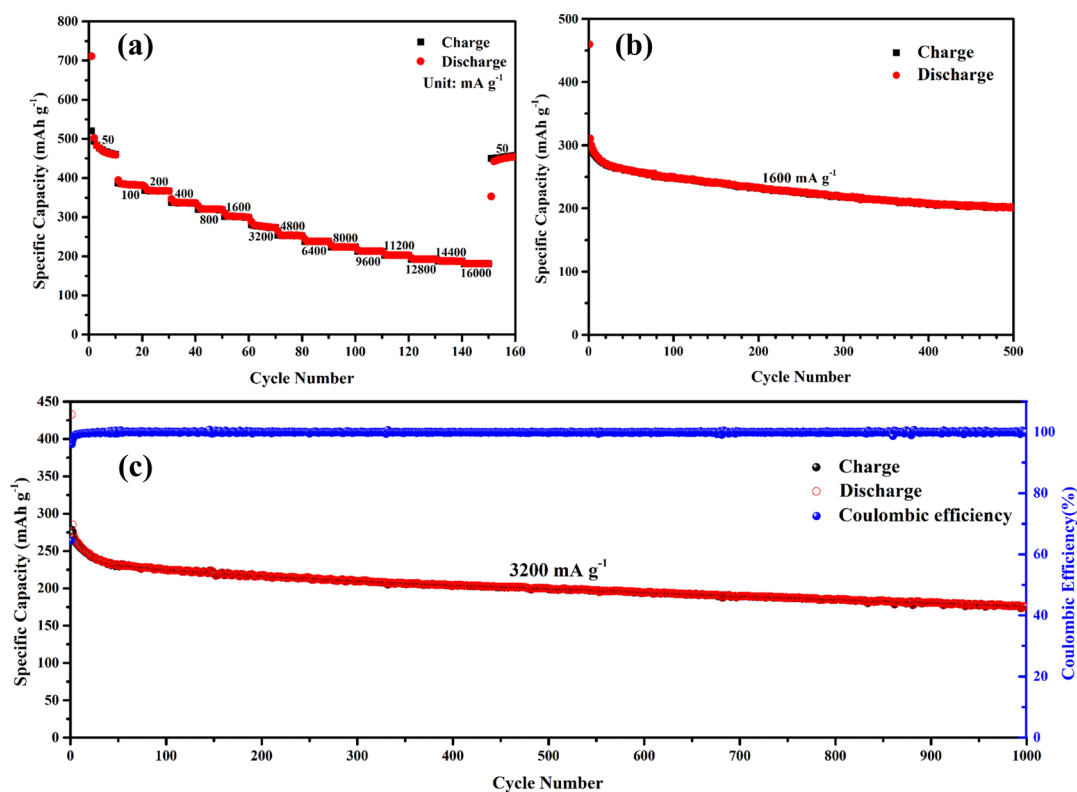
Figure 4. (a) Rate performance at current densities of 50−16,000 mA g^{-1}, (b) cycle performance at a current density of 1600 mA g^{-1}, and (c) rate cycle performance at a current density of 3200 mA g^{-1} for CBC13 carbon black.
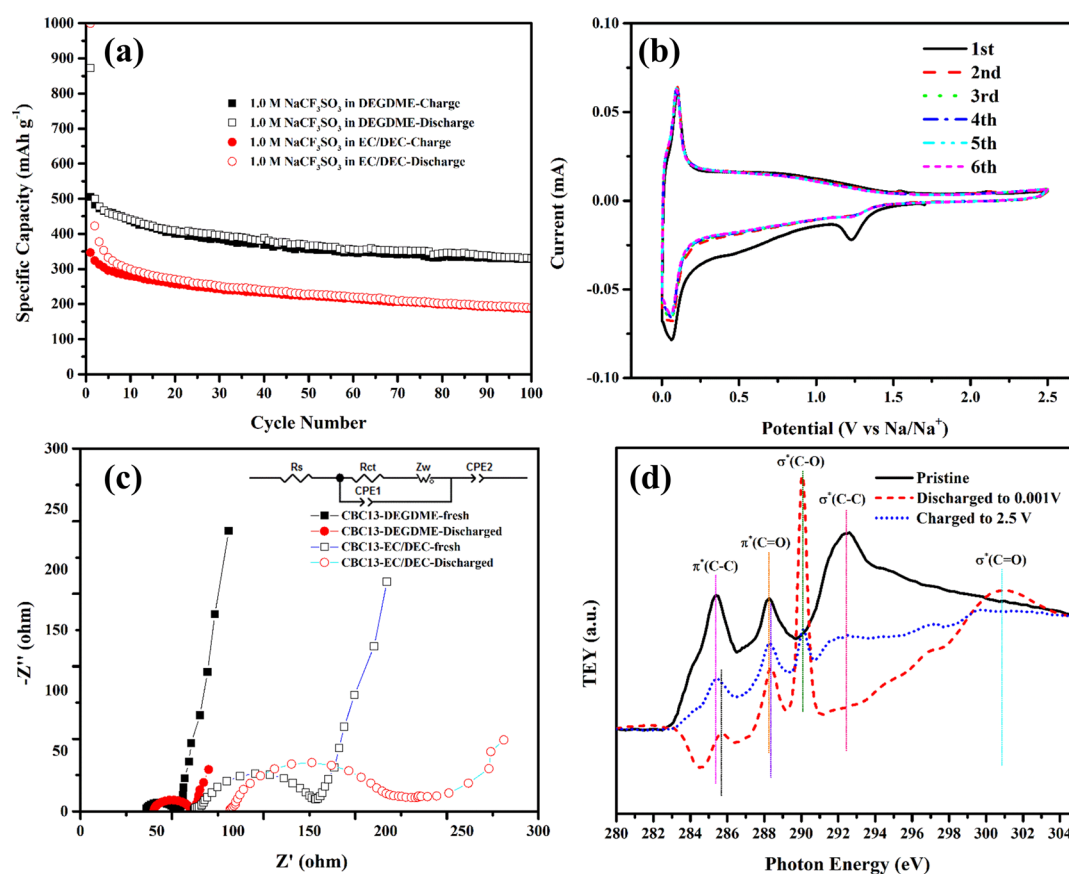
Figure 5. (a) Cycle performances of CBC13 carbon black in different electrolytes using DEGDME and EC/DEC as solvents at a current density of 50 mA g^{-1}. (b) CV curves of CBC13 carbon black in a DEGDME-based electrolyte at 0.1 mV s^{-1}. (c) EIS for CBC13 carbon black electrodes before and after discharging in different electrolytes (the inset shows equivalent circuit model). (d) C K-edge XAS of CBC13 carbon black electrodes at different states when cycled in a DEGDME-based electrolyte.

groups delivers an extremely large reversible capacity of 505 mA h g^{-1} with an initial Coulombic efficiency of 57.9% at 50 mA g^{-1}, but the thermal reducing process could seriously lower the initial charge capacity for CBCH13 to 175 mA h g^{-1} with a 57.4% Coulombic efficiency. Even though the fast capacity fading happens at the beginning of cycling for CBC13 carbon black, it still exhibits reversible capacities of 483, 472, 393, 356, and 341 mA h g^{-1} at the 2nd, 3rd, 25th, 50th, and 75th cycle, respectively, which are much higher than the corresponding results for CBCH13 carbon black. Appealingly, most of the discharged−charged capacities for the functionalized CBC13 carbon black result from the electrochemical intercalation/extraction occurring below 1.5 V, promising its high desirability as an anode material with a high energy density for SIBs. Figure 3b−d further compares the cycle performances of different carbon blacks at various current densities. After 100 cycles at 50 mA g^{-1} as shown in Figure 3b, CBC13 carbon black maintains a reversible capacity of 327 mA h g^{-1} with a 64.8% capacity retention, while N330 and CBCH13 carbon blacks show charge capacities of 196 and 132 mA h g^{-1}, respectively. Admittedly, the rapid capacity decays at first, originating from the slow but complex chemical interactions between oxygenated functionalities and electrolytes during the electrochemical reactions, and it would lead to a comparatively lower value of capacity retention than those of the pristine N330 and CBCH13 carbon blacks. The oxygen-containing functional groups could greatly facilitate the sodium ion diffusion by abundant ionic/electronic pathways and further

enable the subsequent sodiation/desodiation processes by more sodium ion storage sites. When cycled at 100 mA g^{-1} over 100 cycles as shown in Figure 3c, CBC13 carbon black still shows a high charge capacity of 325 mA h g^{-1} with a 73.5% capacity retention, while the reversible capacities of pristine N330 and CBCH13 carbon blacks stabilize around 180 and 127 mA h g^{-1}, respectively. The superior cycle stability for CBC13 carbon black can also be exemplified in Figure 3d with a highly reversible capacity of 256 mA h g^{-1} after 200 cycles at 200 mA g^{-1}, which is much higher than those of the pristine N330 and CBCH13 carbon blacks. Even when cycled at 400 and 800 mA g^{-1} over 100 cycles, the reversible capacities of 287 and 278 mA h g^{-1} could still be obtained for CBC13 carbon black, respectively, as displayed in Figure S16. In contrast to the poor electrochemical performances of the pristine N330 and CBCH13 carbon blacks, the significantly improved capacities of CBC13 carbon black clearly testify the crucial roles of oxygenated functionalities in a highly porous structure, not only facilitating the migrations of electrons/sodium ions through the abundant pathways, but also contributing to the highly efficient sodium ion intercalations/extractions on more active sites. It is necessary to point out both functionalities and porosity have great impacts on the electrochemical properties of carbon blacks, as detailed in the Supporting Information.

In addition to the noticeable reversible capacities, the excellent rate capability and remarkable rate cycle stability can also be recognized for the functionalized carbon black, as

shown in Figure 4. When cycled at the current densities of 50, 100, 200, 400, 800, 1600, and 3200 mA g^{-1}, CBC13 carbon black could deliver charge capacities of 471, 383, 366, 336, 319, 300, and 275 mA h g^{-1}, respectively. Simultaneously, this electrode was also able to maintain highly stable capacities of 253, 238, 224, 213, and 203 mA h g^{-1} at the current densities of 4800, 6400, 8000, 9600, and 11,200 mA g^{-1}, respectively. Interestingly, the large reversible capacities of 193 and 188 mA h g^{-1} could further be achieved for this functionalized electrode at the current densities of 12,800 and 14,400 mA g^{-1}. Even applying an extremely high current density of 16,000 mA g^{-1}, it can still retain a highly reversible capacity of 181 mA h g^{-1} and further regain a large reversible capacity of 453 mA h g^{-1} upon restoring the current density to 50 mA g^{-1}. Impressively, the CBC13 carbon black displays a highly reversible capacity of 202 mA h g^{-1} at 1600 mA g^{-1} over 500 cycles with a 66.44% capacity retention. The outstanding rate cycle performance of 176 mA h g^{-1} with a 0.0369% capacity degradation per cycle and the stable coulombic efficiencies approaching 100% could even be achieved at 3200 mA g^{-1} over 1000 cycles. Specifically, the noticeable electrochemical difference between rate capability and cycle performance for CBC13 carbon black should be attributed to different SEI generation and evolution rates at various current densities, giving rise to different capacity loss at the beginning of cycling. The superior electrochemical reversibility and exceptional rate cycle capability for the functionalized porous carbon outperform the electrochemical properties of several carbonaceous anodes in recent reports.[15,16,22−26,30,31,39,58−61] The ultrafast sodium ion diffusion and electron transport, benefitted from the oxygenated functional groups in a desirable microporous structure with more active sodium ion storage sites, could endow the functionalized carbon black with an ultrahigh rate capability and a highly stable cycle performance. In terms of practical application of carbon anode materials for SIBs, it is quite necessary to testify the electrochemical feasibility of CBC13 carbon black in full cells. In this case, we have initially synthesized a layered P2-Na$_{0.67}$Mn$_{0.9}$Al$_{0.1}$O$_2$ cathode material through a sol−gel method followed by a subsequent high-temperature sintering.[62] When the Na$_{0.67}$Mn$_{0.9}$Al$_{0.1}$O$_2$ cathode material is coupled with the CBC13 anode material at a mass ratio of 1:1.1 in an ether-based electrolyte, the full cell could stably work at a current density of 200 mA g^{-1} in the potential range of 0.5−3.5 V and also retain a large discharging capacity of 78 mA h g^{-1} on the basis of mass for the active cathode material after 50 cycles in Figure S18. Regardless of the relatively poor Coulombic efficiencies at the beginning of cycling, the remarkable electrochemical stability and durability for the Na$_{0.67}$Mn$_{0.9}$Al$_{0.1}$O$_2$/CBC13 full cell further demonstrate a huge application foreground of functionalized porous carbon in practical SIBs.

In terms of carbon anode materials, solvents in electrolytes could also determine the electrochemical sodiation mechanisms and corresponding electrochemical behaviors.[36−38] In the present case, it is necessary to compare the electrochemical properties of functionalized carbon black in ether-based and carbonate-based electrolytes for exploring the structural evolution of SEI during the discharging/charging processes. In Figure 5a, CBC13 carbon black in the EC/DEC-based electrolyte could only present an initial reversible capacity of 347 mA h g^{-1} with a low coulombic efficiency of 34.7% and a poor capacity retention of 53.6% after 100 cycles at 50 mA g^{-1}. The superior electrochemical performance for DEGDME-based electrolyte can also be found in CBCH30 carbon black with a highly stable capacity of 244 mA h g^{-1} at 50 mA g^{-1} over 100 cycles, as shown in Figure S29. A lower reversible capacity and a faster capacity decay for carbon black in the EC/DEC-based electrolyte should be ascribed to its sole dependence on sodium ion insertion into the disordered structures and uncontrollable accumulations of a thick SEI layer. Comparatively, the DEGDME-based electrolyte enables the functionalized porous carbon to fully utilize the potential capacity via a synergistic combination of sodium ion insertion into the disordered regions with solvated sodium ion compound cointercalation into the graphitic structure. With the assistance of an ether-based electrolyte, the functionalized porous carbon could take full advantage of accessible graphitic regions and disordered structures to boost the sodium storage process upon electrochemical reactions.[42,43] Intriguingly, a sharp anodic peak appeared around 0.5 V during the first discharging process for CBC13 carbon black in the EC/DEC-based electrolyte, as shown in Figure S19, which does not arise in the same process for DEGDME-based electrolyte in Figure 5b, hinting at a distinct SEI formation route for the functionalized carbon black in the ether-based electrolyte. At the same time, the negligible differences for intensities and positions of all cathodic/anodic peaks below 0.5 V in the following cycles further prove a high electrochemical reversibility of functionalized carbon black. Furthermore, the comparisons of EIS in Figure 5c and related parameters in Table S4 for the pristine and discharged electrodes in different electrolytes also verify the electrochemical advantages of ether-based electrolytes. Owing to the uncontrollable generation of a thick SEI layer on the surface of CBC13 carbon electrode upon discharging in the EC/DEC-based electrolyte, its charge transfer resistance would significantly increase, while the corresponding value in the DEGDME-based electrolyte slightly changed. Additionally, the SEI impedance for the discharged electrode in the EC/DEC-based electrolyte is much higher than that for DEGDME-based electrolyte, implying the limited formation of a robust but thin SEI layer on the CBC13 carbon electrode in the DEGDME-based electrolyte. On the one hand, the unconstrained generation of a thick SEI layer in the EC/DEC-based electrolyte would severely lower the initial reversibility/coulombic efficiency, sacrifice the electrolyte, and inhibit the facile diffusion of sodium ions. On the other hand, the self-limited emergence of a robust and thin SEI layer in the DEGDME-based electrolyte could effectively stabilize the fragile carbon structure, accommodate the expanded structure in discharged carbon, and further promote the rapid migrations of sodium ions/solvated compounds.[40,41]

The formation and evolution of SEI on CBC13 carbon black electrodes in the DEGDME-based electrolyte were also investigated by the highly surface-sensitive C K-edge XAS in the TEY mode, as shown in Figure 5d. For the pristine CBC13 carbon black, two obvious features at 285.4 and 292.4 eV should correspond to the transitions of C 1s electrons toward the π^*(C−C) and σ^*(C−C) orbitals,[63] respectively, while the peak at 288.2 eV is related to the π^*(C=O) transitions.[63−66] Upon discharging to 0.001 V, the peaks for the π^*(C−C) and π^*(C=O) transitions shift negatively, and the σ^*(C−C) feature completely disappears. Importantly, a newly formed sharp peak around 290.0 eV attributed to the σ^*(C−O) transitions for the oxygen-containing functional groups[51,66,67] and a broad peak around 301.0 eV as the σ^*(C=O) feature[51,67,68] can be clearly identified in the XAS measure-
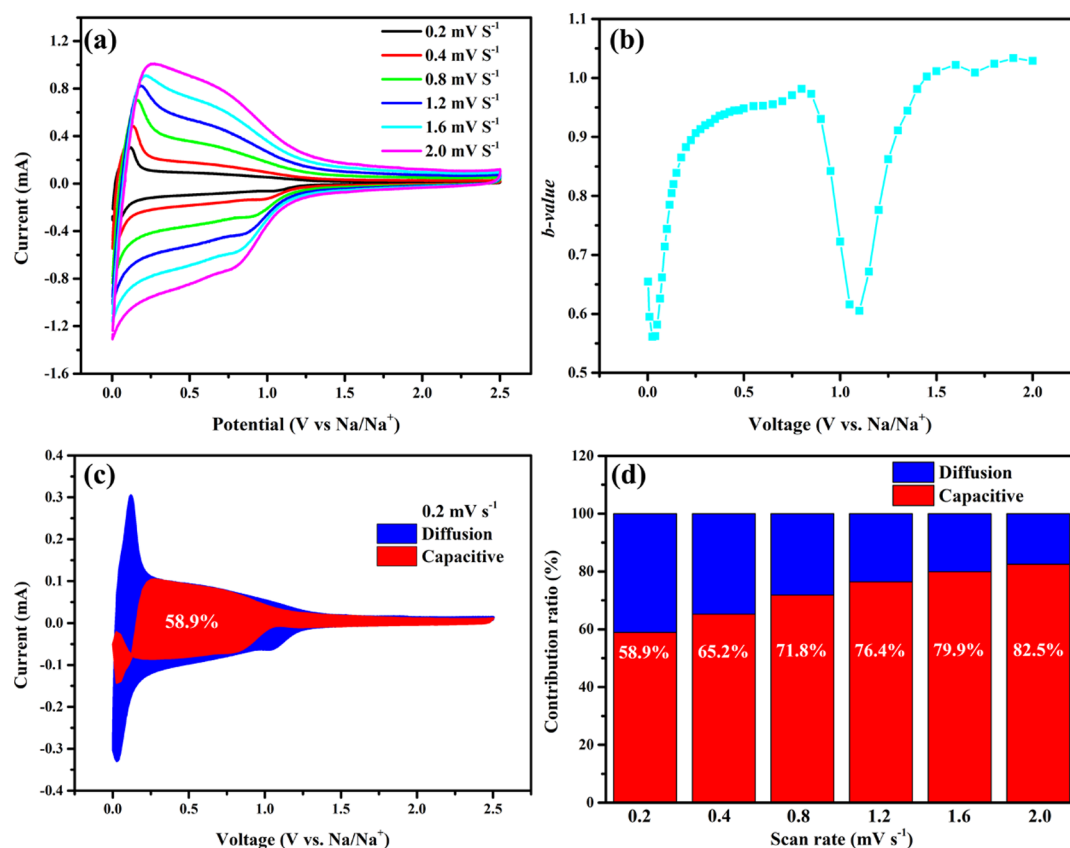
Figure 6. (a) CV curves of CBC13 carbon black at various scan rates. (b) Calculated *b*-values plotted against the battery potentials for CBC13 carbon black in the cathodic (sodiation) process. (c) Capacitive contribution at a scan rate of 0.2 mV s⁻¹. (d) Contribution ratios of capacitive capacity at various scan rates.

ment, as a strong evidence for electrolyte decomposition and subsequent SEI generation. When charged the electrode back to 2.5 V, the $\pi*(C-C)$ feature moves to the initial position at 285.4 eV, and the peak for $\sigma(C-C)*$ transition reappears around 292.4 eV. Noticeably, the $\pi*(C=O)$ peak does not change its position and intensity, while the $\sigma*(C-O)$ feature still maintains its previous position but with a comparatively lower intensity. The persistence of the $\sigma*(C-O)$ feature and irreversibility of the $\pi*(C=O)$ peak elucidate the preservation of a robust SEI thin layer, which could not only efficiently facilitate the migration of sodium ions and solvated compounds in the electrolyte/interphase/electrode, but also effectively accommodate the volume variations during the cycling and further avoid the overconsumption of electrolyte, leading to a highly reversible capacity and an exceptional rate capability.

While the diffusion-controlled intercalations of sodium ions/ solvated sodium ion species into graphitic/disordered structures would primarily determine the electrochemical properties of CBC13 carbon black, the surface-induced capacitive reactions by absorbing these species into cavities/ nanopores would also play a vital role in the charge storage process of carbon anode materials for SIBs.[26,40,69,70] Consequently, the CV measurements at various scan rates in Figure 6a were conducted to accurately quantify the diffusive/ capacitive contributions and further clarify the sodium storage mechanism during the sodiation/desodiation processes. Theoretically, the relationship of current response with scan rate can be expressed by a classical power-law formula

$$i(V) = av^b \tag{1}$$

where $i(V)$ (mA) is an absolute value of current response at a specific voltage of V and a corresponding scan rate of v (mV s⁻¹), while a and b are adjustable values. On the basis of a simple linear fitting of the $\log(|i(V)|)$ versus $\log(v)$ plot, the b value can be easily obtained for a specific potential at a certain scan rate. It has been generally recognized that a b value of 0.5 represents a typical diffusion-controlled intercalation reaction, and the b value of 1.0 in a linear relationship of current response with scan rate further corresponds to a capacitance-dominated charge storage. As displayed in Figure 6b, 50 data points were selected to calculate the b values for CBC13 carbon black at different potentials in the sodiation process between 0.001 and 2.0 V. Interestingly, the b value would initially approach 1.0 above 1.4 V, then rapidly drop to 0.6 at 1.1 V, subsequently increasing to 0.98 at 0.8 V, and finally decreasing to 0.59 at 0.01 V, indicating the electrochemical dominances of capacitive reactions at high/medium voltages (>1.4 and 1.0−0.1 V) and intercalation reactions at relatively low voltages (<0.1 V) with particular diffusion-controlled reactions around 1.1 V. Simultaneously, the flat CV curves with a rectangular shape at high voltages for various scan rates also prove the leading function of capacitive contribution in sodium storage, while the presence of cathodic/anodic peaks in redox reactions at low voltages further exhibit the dominant role of diffusive contribution in charge storage. Even though the voltage shift for anodic peaks from 0.2 to 2.0 mV s⁻¹ could reach a relatively large value of 0.14 V, the cathodic peaks barely changed the voltage position, hinting a low electro-

chemical polarization and a desirable reaction kinetics upon sodiation. On the basis of eq 1, the contribution ratios of capacitive and diffusive reactions can be calculated by the following equation

$$i(V) = k_1 v + k_2 v^{1/2} \tag{2}$$

where $k_1 v$ at a b value of 1.0 represents the capacitive contribution from surface reactions, and $k_2 v^{1/2}$ at a b value of 0.5 corresponds to the diffusive contribution from intercalation reactions in current response at a specific potential. Through a linear fitting of $i(V)/v^{1/2}$ versus $v^{1/2}$ profile at a certain potential for a fixed scan rate, the corresponding value of k_1 can be immediately acquired, while various k_1 values could be further plotted against different potentials, resulting in the corresponding capacitive contributions at various scan rates. When characterized at a scan rate of 0.2 mV s^{-1}, the CBC13 carbon black would deliver a dominating capacitive contribution of 58.9% in Figure 6c, while the corresponding contribution areas are consistent with the predictions of b values. As shown in Figures 6d and S22b−f, this key parameter would continuously increase to 65.2, 71.8, 76.4, 79.9, and 82.5% at scan rates of 0.4, 0.8, 1.2, 1.6, and 2.0 mV s^{-1}, respectively, demonstrating the strong capability of surface oxygenated functionalities to facilitate the rapid migrations of sodium ions/solvated sodium ion compounds and boost the electrochemical performances of CBC13 carbon black. To understand the reaction kinetics of various carbon blacks upon sodiation/desodiation, the galvanostatic intermittent titration technique (GITT) measurements in Figure S35a−c were also carried out to calculate the Na$^+$ diffusion coefficients during the discharging and charging processes via a specific equation in Fick's second law. Apparently, the Na$^+$ diffusion coefficients for CBC13 carbon black are much higher than the corresponding parameters for CBCH13 and N330 carbon blacks in Figure S35d,e, hinting at a superior reaction kinetics for functionalized porous carbon black.

With the assistance of an advantageously synergistic mechanism for sodium storage in ether-based electrolytes toward carbon anode materials, the oxygenated functionalities could not only generate abundant pathways for migrations of sodium ions/solvated sodium ion species, but also ensure a fast capacitive reaction on the defective surface, contributing to an exceptional reversible capacity and an excellent rate performance. Meanwhile, the controllable formation of a robust and thin SEI layer with the subsequent preservation would further stabilize the fragile porous structure for the functionalized carbon black. The functionalized porous carbon with a superior cycle performance at exceptionally high rates is very desirable for applications in large-scale grid energy storage with strict requirements of a high energy density and a quick storage response.

4. CONCLUSIONS

In summary, the functionalized porous carbon black derived from a CO$_2$ thermal etching route was successfully applied as a high-performance anode material for SIBs. Benefitting from its abundant oxygenated functionalities and the desirable microporosity with the obvious pseudocapacitive behaviors, the etched carbon black could deliver an extremely large reversible capacity (505 mA h g^{-1} at 50 mA g^{-1}), an outstanding cycle stability (176 mA h g^{-1} at 3200 mA g^{-1} after 1000 cycles), and an exceptional rate capability (181 mA h g^{-1} at 16,000 mA

g^{-1}). As unearthed by the electrochemical and physicochemical characterizations, the controllable formation and subsequent preservation of a robust but thin SEI film in the electrochemical reactions, could not only facilitate the migrations of sodium ions and solvated sodium ion species, but also stabilize the fragile structure for porous carbon materials upon the sodium ion intercalation/extraction processes. At the same time, the surface-induced capacitive reactions on the defective surface would significantly contribute to the charge storage process upon sodiation. The novelty of oxygenated functionalities on the promotion of sodium storage capability and the advantage of ether-based electrolytes on a controllable generation of a SEI thin film have directly opened up a new avenue for developing high-capacity and long-life carbon anode materials for SIBs.

■ ASSOCIATED CONTENT

Ⓢ Supporting Information

The Supporting Information is available free of charge at https://pubs.acs.org/doi/10.1021/acsami.0c08899.

> Physical and chemical properties for CBC13 carbon black, CBC carbon blacks, and CBCH carbon blacks; electrochemical properties for CBC13 carbon black, CBC carbon blacks, and CBCH carbon blacks; electrochemical comparison of CBC13 carbon black with reported results (PDF)

■ AUTHOR INFORMATION

Corresponding Authors

Tsun-Kong Sham − *Department of Chemistry, University of Western Ontario, London, Ontario N6A 5B7, Canada;* ⓘ orcid.org/0000-0003-1928-6697; Email: tsham@uwo.ca

Xueliang Sun − *Department of Mechanical & Materials Engineering, University of Western Ontario, London, Ontario N6A 5B9, Canada;* ⓘ orcid.org/0000-0003-0374-1245; Email: xsun9@uwo.ca

Authors

Wei Xiao − *Department of Mechanical & Materials Engineering and Department of Chemistry, University of Western Ontario, London, Ontario N6A 5B9, Canada; Institute of Advanced Electrochemical Energy & School of Materials Science and Engineering, Xi'an University of Technology, Xi'an, Shaanxi 710048, China*

Qian Sun − *Department of Mechanical & Materials Engineering, University of Western Ontario, London, Ontario N6A 5B9, Canada*

Jian Liu − *Department of Mechanical & Materials Engineering, University of Western Ontario, London, Ontario N6A 5B9, Canada*

Biwei Xiao − *Department of Mechanical & Materials Engineering, University of Western Ontario, London, Ontario N6A 5B9, Canada*

Xia Li − *Department of Mechanical & Materials Engineering, University of Western Ontario, London, Ontario N6A 5B9, Canada*

Per-Anders Glans − *Lawrence Berkeley National Laboratory, Advanced Light Source, Berkeley, California 94720, United States*

Jun Li − *Department of Chemistry, University of Western Ontario, London, Ontario N6A 5B7, Canada*

Ruying Li − *Department of Mechanical & Materials Engineering, University of Western Ontario, London, Ontario N6A 5B9, Canada*

Xifei Li − *Institute of Advanced Electrochemical Energy & School of Materials Science and Engineering, Xi'an University of Technology, Xi'an, Shaanxi 710048, China*

Jinghua Guo − *Lawrence Berkeley National Laboratory, Advanced Light Source, Berkeley, California 94720, United States;* ● orcid.org/0000-0002-8576-2172

Wanli Yang − *Lawrence Berkeley National Laboratory, Advanced Light Source, Berkeley, California 94720, United States;* ● orcid.org/0000-0003-0666-8063

Complete contact information is available at:
https://pubs.acs.org/10.1021/acsami.0c08899

Author Contributions

W.X. designed the experiment, conducted the data analysis, and wrote the manuscript. Q.S. designed the experiment, organized the writing structure, and revised the manuscript. Jian Liu and P.-A.G. collected the synchrotron data from Advanced Light Sources. Jun Li provided the suggestions for synchrotron data analysis and manuscript writing. Xifei Li provided the suggestions for electrochemical data analysis and manuscript writing. B.X., Xia Li, and R.L. carried out the general characterizations in the laboratory. J.G. and W.Y. directed the synchrotron data collection at Advanced Light Sources. T.-K.S. analyzed the synchrotron data and contributed to the manuscript writing. X.S. conceived the idea and contributed to the manuscript writing. All authors discussed the experimental results and proofed the final manuscript.

Notes

The authors declare no competing financial interest.

■ REFERENCES

(1) Armand, M.; Tarascon, J.-M. Building Better Batteries. *Nature* **2008**, *451*, 652−657.

(2) Larcher, D.; Tarascon, J.-M. Towards Greener and More Sustainable Batteries for Electrical Energy Storage. *Nat. Chem.* **2015**, *7*, 19−29.

(3) Tarascon, J.-M.; Armand, M. Issues and Challenges Facing Rechargeable Lithium Batteries. *Nature* **2001**, *414*, 359−367.

(4) Slater, M. D.; Kim, D.; Lee, E.; Johnson, C. S. Sodium-Ion Batteries. *Adv. Funct. Mater.* **2013**, *23*, 947−958.

(5) Palomares, V.; Serras, P.; Villaluenga, I.; Hueso, K. B.; Carretero-González, J.; Rojo, T. Na-Ion Batteries, Recent Advances and Present Challenges to Become Low Cost Energy Storage Systems. *Energy Environ. Sci.* **2012**, *5*, 5884−5901.

(6) Yabuuchi, N.; Kubota, K.; Dahbi, M.; Komaba, S. Research Development On Sodium-Ion Batteries. *Chem. Rev.* **2014**, *114*, 11636−11682.

(7) Kundu, D.; Talaie, E.; Duffort, V.; Nazar, L. F. The Emerging Chemistry of Sodium Ion Batteries for Electrochemical Energy Storage. *Angew. Chem., Int. Ed.* **2015**, *54*, 3431−3448.

(8) Pan, H.; Hu, Y.-S.; Chen, L. Room-Temperature Stationary Sodium-Ion Batteries for Large-Scale Electric Energy Storage. *Energy Environ. Sci.* **2013**, *6*, 2338−2360.

(9) Fang, Y.; Xiao, L.; Chen, Z.; Ai, X.; Cao, Y.; Yang, H. Recent Advances in Sodium-Ion Battery Materials. *Electrochem. Energy Rev.* **2018**, *1*, 294−323.

(10) Wang, T.; Su, D.; Shanmukaraj, D.; Rojo, T.; Armand, M.; Wang, G. Electrode Materials for Sodium-Ion Batteries: Considerations on Crystal Structures and Sodium Storage Mechanisms. *Electrochem. Energy Rev.* **2018**, *1*, 200−237.

(11) Yang, Z.; Zhang, J.; Kintner-Meyer, M. C. W.; Lu, X.; Choi, D.; Lemmon, J. P.; Liu, J. Electrochemical Energy Storage for Green Grid. *Chem. Rev.* **2011**, *111*, 3577−3613.

(12) Ge, X.; Liu, S.; Qiao, M.; Du, Y.; Li, Y.; Bao, J.; Zhou, X. Enabling Superior Electrochemical Properties for Highly Efficient Potassium Storage by Impregnating Ultrafine Sb Nanocrystals within Nanochannel-Containing Carbon Nanofibers. *Angew. Chem., Int. Ed.* **2019**, *58*, 14578−14583.

(13) Ge, P.; Fouletier, M. Electrochemical Intercalation of Sodium in Graphite. *Solid State Ionics* **1988**, *28−30*, 1172−1175.

(14) Doeff, M. M.; Ma, Y.; Visco, S. J.; Jonghe, L. C. D. Electrochemical Insertion of Sodium into Carbon. *J. Electrochem. Soc.* **1993**, *140*, L169−L170.

(15) Li, Y.; Hu, Y.−S.; Qi, X.; Rong, X.; Li, H.; Huang, X.; Chen, L. Advanced Sodium-Ion Batteries Using Superior Low Cost Pyrolyzed Anthracite Anode: Towards Practical Applications. *Energy Storage Mater.* **2016**, *5*, 191−197.

(16) Liu, P.; Li, Y.; Hu, Y.-S.; Li, H.; Chen, L.; Huang, X. A Waste Biomass Derived Hard Carbon as a High-Performance Anode Material for Sodium-Ion Batteries. *J. Mater. Chem. A* **2016**, *4*, 13046−13052.

(17) Bai, P.; He, Y.; Zou, X.; Zhao, X.; Xiong, P.; Xu, Y. Elucidation of the Sodium-Storage Mechanism in Hard Carbons. *Adv. Energy Mater.* **2018**, *8*, 1703217.

(18) Luo, W.; Schardt, J.; Bommier, C.; Wang, B.; Razink, J.; Simonsen, J.; Ji, X. Carbon Nanofibers Derived from Cellulose Nanofibers as a Long-Life Anode Material for Rechargeable Sodium-Ion Batteries. *J. Mater. Chem. A* **2013**, *1*, 10662−10666.

(19) Ding, J.; Wang, H.; Li, Z.; Kohandehghan, A.; Cui, K.; Xu, Z.; Zahiri, B.; Tan, X.; Lotfabad, E. M.; Olsen, B. C.; Mitlin, D. Carbon Nanosheet Frameworks Derived from Peat Moss as High Performance Sodium Ion Battery Anodes. *ACS Nano* **2013**, *7*, 11004−11015.

(20) Chen, T.; Liu, Y.; Pan, L.; Lu, T.; Yao, Y.; Sun, Z.; Chua, D. H. C.; Chen, Q. Electrospun Carbon Nanofibers as Anode Material for Sodium Ion Batteries with Excellent Cycle Performance. *J. Mater. Chem. A* **2014**, *2*, 4117−4121.

(21) Hou, H.; Banks, C. E.; Jing, M.; Zhang, Y.; Ji, X. Carbon Quantum Dots and Their Derivative 3D Porous Carbon Frameworks for Sodium-Ion Batteries with Ultralong Cycle Life. *Adv. Mater.* **2015**, *27*, 7861−7866.

(22) Li, Y.; Hu, Y.-S.; Titirici, M.-M.; Chen, L.; Huang, X. Hard Carbon Microtubes Made from Renewable Cotton as High-Performance Anode Material for Sodium-Ion Batteries. *Adv. Energy Mater.* **2016**, *6*, 1600659.

(23) Yang, J.; Zhou, X.; Wu, D.; Zhao, X.; Zhou, Z. S-Doped N-Rich Carbon Nanosheets with Expanded Interlayer Distance as Anode Materials for Sodium-Ion Batteries. *Adv. Mater.* **2017**, *29*, 1604108.

(24) Bin, D.-S.; Li, Y.; Sun, Y.-G.; Duan, S.-Y.; Lu, Y.; Ma, J.; Cao, A.-M.; Hu, Y.-S.; Wan, L.-J. Structural Engineering of Multishelled Hollow Carbon Nanostructures for High-Performance Na-Ion Battery Anode. *Adv. Energy Mater.* **2018**, *8*, 1800855.

(25) Zhang, F.; Alhajji, E.; Lei, Y.; Kurra, N.; Alshareef, H. N. Highly Doped 3D Graphene Na-Ion Battery Anode by Laser Scribing Polyimide Films in Nitrogen Ambient. *Adv. Energy Mater.* **2018**, *8*, 1800353.

(26) Yao, X.; Ke, Y.; Ren, W.; Wang, X.; Xiong, F.; Yang, W.; Qin, M.; Li, Q.; Mai, L. Defect-Rich Soft Carbon Porous Nanosheets for Fast and High-Capacity Sodium-Ion Storage. *Adv. Energy Mater.* **2019**, *9*, 1803260.

(27) Xu, J.; Wang, M.; Wickramaratne, N. P.; Jaroniec, M.; Dou, S.; Dai, L. High-Performance Sodium Ion Batteries Based on Three-Dimensional Anode from Nitrogen-Doped Graphene Foams. *Adv. Mater.* **2015**, *27*, 2042−2048.

(28) Yang, F.; Zhang, Z.; Du, K.; Zhao, X.; Chen, W.; Lai, Y.; Li, J. Dopamine Derived Nitrogen-Doped Carbon Sheets as Anode Materials for High-Performance Sodium Ion Batteries. *Carbon* **2015**, *91*, 88−95.

(29) Wang, P.; Qiao, B.; Du, Y.; Li, Y.; Zhou, X.; Dai, Z.; Bao, J. Fluorine-Doped Carbon Particles Derived from Lotus Petioles as High-Performance Anode Materials for Sodium-Ion Batteries. *J. Phys. Chem. C* **2015**, *119*, 21336−21344.

(30) Yoon, D.; Kim, D. H.; Chung, K. Y.; Chang, W.; Kim, S. M.; Kim, J. Hydrogen-Enriched Porous Carbon Nanosheets with High Sodium Storage Capacity. *Carbon* **2016**, *98*, 213−220.

(31) Li, Z.; Bommier, C.; Chong, Z. S.; Jian, Z.; Surta, T. W.; Wang, X.; Xing, Z.; Neuefeind, J. C.; Stickle, W. F.; Dolgos, M.; Greaney, P. A.; Ji, X. Mechanism of Na-Ion Storage in Hard Carbon Anodes Revealed by Heteroatom Doping. *Adv. Energy Mater.* **2017**, *7*, 1602894.

(32) Wang, Q.; Ge, X.; Xu, J.; Du, Y.; Zhao, X.; Si, L.; Zhou, X. Fabrication of Microporous Sulfur-Doped Carbon Microtubes for High-Performance Sodium-Ion Batteries. *ACS Appl. Energy Mater.* **2018**, *1*, 6638−6645.

(33) Ponrouch, A.; Marchante, E.; Courty, M.; Tarascon, J.-M.; Palacín, M. R. In Search of an Optimized Electrolyte for Na-Ion Batteries. *Energy Environ. Sci.* **2012**, *5*, 8572.

(34) Ponrouch, A.; Dedryvère, R.; Monti, D.; Demet, A. E.; Ateba Mba, J. M.; Croguennec, L.; Masquelier, C.; Johansson, P.; Palacín, M. R. Towards High Energy Density Sodium Ion Batteries through Electrolyte Optimization. *Energy Environ. Sci.* **2013**, *6*, 2361−2369.

(35) Liu, Z. Insight into Effects of Fluoroethylene Carbonate Additive on the Cathode in Sodium Ion Batteries. *Acta Phys. -Chim. Sin.* **2019**, *35*, 804−805.

(36) Jache, B.; Adelhelm, P. Use of Graphite as a Highly Reversible Electrode with Superior Cycle Life for Sodium-Ion Batteries by Making Use of Co-Intercalation Phenomena. *Angew. Chem., Int. Ed.* **2014**, *53*, 10169−10173.

(37) Kim, H.; Hong, J.; Park, Y.-U.; Kim, J.; Hwang, I.; Kang, K. Sodium Storage Behavior in Natural Graphite using Ether-based Electrolyte Systems. *Adv. Funct. Mater.* **2014**, *25*, 534−541.

(38) Kim, H.; Hong, J.; Yoon, G.; Kim, H.; Park, K.-Y.; Park, M.-S.; Yoon, W.-S.; Kang, K. Sodium Intercalation Chemistry In Graphite. *Energy Environ. Sci.* **2015**, *8*, 2963−2969.

(39) Zhu, Y.-E.; Yang, L.; Zhou, X.; Li, F.; Wei, J.; Zhou, Z. Boosting the Rate Capability of Hard Carbon with an Ether-Based Electrolyte for Sodium Ion Batteries. *J. Mater. Chem. A* **2017**, *5*, 9528−9532.

(40) Zhang, J.; Wang, D.-W.; Lv, W.; Zhang, S.; Liang, Q.; Zheng, D.; Kang, F.; Yang, Q.-H. Achieving Superb Sodium Storage Performance on Carbon Anodes through An Ether-Derived Solid Electrolyte Interphase. *Energy Environ. Sci.* **2017**, *10*, 370−376.

(41) Goktas, M.; Bolli, C.; Berg, E. J.; Novák, P.; Pollok, K.; Langenhorst, F.; Roeder, M. v.; Lenchuk, O.; Mollenhauer, D.; Adelhelm, P. Graphite as Cointercalation Electrode for Sodium-Ion Batteries: Electrode Dynamics and the Missing Solid Electrolyte Interphase (SEI). *Adv. Energy Mater.* **2018**, *8*, 1702724.

(42) Xiao, W.; Sun, Q.; Liu, J.; Xiao, B.; Glans, P.-A.; Li, J.; Li, R.; Guo, J.; Yang, W.; Sham, T.-K.; Sun, X. Utilizing the Full Capacity of Carbon Black as Anode for Na-Ion Batteries via Solvent Co-Intercalation. *Nano Res.* **2017**, *10*, 4378−4387.

(43) Xiao, W.; Sun, Q.; Liu, J.; Xiao, B.; Liu, Y.; Glans, P.-A.; Li, J.; Li, R.; Li, X.; Guo, J.; Yang, W.; Sham, T.-K.; Sun, X. Boosting the Sodium Storage Behaviors of Carbon Materials in Ether-Based Electrolyte through the Artificial Manipulation of Microstructure. *Nano Energy* **2019**, *66*, 104177.

(44) Bommier, C.; Mitlin, D.; Ji, X. Internal Structure-Na Storage Mechanisms-Electrochemical Performance Relations in Carbons. *Prog. Mater. Sci.* **2018**, *97*, 170−203.

(45) Li, Y.; Li, X.; Geng, D.; Tang, Y.; Li, R.; Dodelet, J.-P.; Lefèvre, M.; Sun, X. Carbon Black Cathodes for Lithium Oxygen Batteries: Influence of Porosity and Heteroatom-Doping. *Carbon* **2013**, *64*, 170−177.

(46) Li, Y.; Hu, Y.-S.; Li, H.; Chen, L.; Huang, X. A Superior Low-Cost Amorphous Carbon Anode Made from Pitch and Lignin for Sodium-Ion Batteries. *J. Mater. Chem. A* **2016**, *4*, 96−104.

(47) Li, Y.; Mu, L.; Hu, Y.-S.; Li, H.; Chen, L.; Huang, X. Pitch-Derived Amorphous Carbon as High Performance Anode for Sodium-Ion Batteries. *Energy Storage Mater.* **2016**, *2*, 139−145.

(48) Zhang, Z.; Pfefferle, L.; Haller, G. L. Comparing Characterization of Functionalized Multi-Walled Carbon Nanotubes by Potentiometric Proton Titration, NEXAFS, and XPS. *Chin. J. Catal.* **2014**, *35*, 856−863.

(49) Jeong, H.-K.; Noh, H.-J.; Kim, J.-Y.; Jin, M. H.; Park, C. Y.; Lee, Y. H. X-Ray Absorption Spectroscopy of Graphite Oxide. *Europhys. Lett.* **2008**, *82*, 67004.

(50) Lee, V.; Whittaker, L.; Jaye, C.; Baroudi, K. M.; Fischer, D. A.; Banerjee, S. Large-Area Chemically Modified Graphene Films: Electrophoretic Deposition and Characterization by Soft X-ray Absorption Spectroscopy. *Chem. Mater.* **2009**, *21*, 3905−3916.

(51) Banerjee, S.; Hemraj-Benny, T.; Balasubramanian, M.; Fischer, D. A.; Misewich, J. A.; Wong, S. S. Ozonized Single-Walled Carbon Nanotubes Investigated Using NEXAFS Spectroscopy. *Chem. Commun.* **2004**, 772−773.

(52) Luo, D.; Xu, J.; Guo, Q.; Fang, L.; Zhu, X.; Xia, Q.; Xia, H. Surface-Dominated Sodium Storage Towards High Capacity and Ultrastable Anode Material for Sodium-Ion Batteries. *Adv. Funct. Mater.* **2018**, *28*, 1805371.

(53) He, Y.; Bai, P.; Gao, S.; Xu, Y. Marriage of an Ether-Based Electrolyte with Hard Carbon Anodes Creates Superior Sodium-Ion Batteries with High Mass Loading. *ACS Appl. Mater. Interfaces* **2018**, *10*, 41380−41388.

(54) Haerle, R.; Riedo, E.; Pasquarello, A.; Baldereschi, A. sp2/sp3 Hybridization Ratio in Amorphous Carbon from C1 Score-Level Shifts: X-Ray Photoelectron Spectroscopy and First-Principles Calculation. *Phys. Rev. B: Condens. Matter Mater. Phys.* **2002**, *65*, 451011.

(55) Lü, H.-Y.; Zhang, X.-H.; Wan, F.; Liu, D.-S.; Fan, C.-Y.; Xu, H.-M.; Wang, G.; Wu, X.-L. Flexible P-Doped Carbon Cloth: Vacuum-Sealed Preparation and Enhanced Na-Storage Properties as Binder-Free Anode for Sodium Ion Batteries. *ACS Appl. Mater. Interfaces* **2017**, *9*, 12518−12527.

(56) Hou, H.; Shao, L.; Zhang, Y.; Zou, G.; Chen, J.; Ji, X. Large-Area Carbon Nanosheets Doped with Phosphorus: A High-Performance Anode Material for Sodium-Ion Batteries. *Adv. Sci.* **2017**, *4*, 1600243.

(57) Liu, S.; Zhou, J.; Song, H. 2D Zn-Hexamine Coordination Frameworks and Their Derived N-Rich Porous Carbon Nanosheets for Ultrafast Sodium Storage. *Adv. Energy Mater.* **2018**, *8*, 1800569.

(58) Bai, P.; He, Y.; Xiong, P.; Zhao, X.; Xu, K.; Xu, Y. Long Cycle Life and High Rate Sodium-Ion Chemistry for Hard Carbon Anodes. *Carbon* **2018**, *13*, 274−282.

(59) Xiao, B.; Soto, F. A.; Gu, M.; Han, K. S.; Song, J.; Wang, H.; Engelhard, M. H.; Murugesan, V.; Mueller, K. T.; Reed, D.; Sprenkle, V. L.; Balbuena, P. B.; Li, X. Lithium-Pretreated Hard Carbon as High-Performance Sodium-Ion Battery Anodes. *Adv. Energy Mater.* **2018**, *8*, 1801441.

(60) Xie, F.; Xu, Z.; Jensen, A. C. S.; Au, H.; Lu, Y.; Araullo-Peters, V.; Drew, A. J.; Hu, Y. S.; Titirici, M. M. Hard-Soft Carbon Composite Anodes with Synergistic Sodium Storage Performance. *Adv. Funct. Mater.* **2019**, *29*, 1901072.

(61) Pei, Z.; Meng, Q.; Wei, L.; Fan, J.; Chen, Y.; Zhi, C. Toward Efficient and High Rate Sodium-Ion Storage: A New Insight from Dopant-Defect Interplay in Textured Carbon Anode Materials. *Energy Storage Mater.* **2020**, *28*, 55−63.

(62) Liu, X.; Zuo, W.; Zheng, B.; Xiang, Y.; Zhou, K.; Xiao, Z.; Shan, P.; Shi, J.; Li, Q.; Zhong, G.; Fu, R.; Yang, Y. P2-$Na_{0.67}Al_xMn_{1-x}O_2$: Cost-Effective, Stable and High-Rate Sodium Electrodes by Suppressing Phase Transitions and Enhancing Sodium Cation Mobility. *Angew. Chem., Int. Ed.* **2019**, *58*, 18086−18095.

(63) Zhou, J.; Zhou, X.; Li, R.; Sun, X.; Ding, Z.; Cutler, J.; Sham, T.-K. Electronic Structure and Luminescence Center of Blue Luminescent Carbon Nanocrystals. *Chem. Phys. Lett.* **2009**, *474*, 320−324.

(64) Zhou, J.; Zhou, X.; Sun, X.; Li, R.; Murphy, M.; Ding, Z.; Sun, X.; Sham, T.-K. Interaction between Pt Nanoparticles and Carbon Nanotubes-An X-Ray Absorption Near Edge Structures (XANES) Study. *Chem. Phys. Lett.* **2007**, *437*, 229−232.

(65) Bouchet-Fabre, B.; Pinault, M.; Pichot, V.; Launois, P.; Mayne-L'Hermite, M.; Parent, P.; Laffon, K.; Durand, D.; Reynaud, C. NEXAFS and X-Ray Scattering Study of Structure Shanges after Post-Annealing Treatments of Aligned MWNTs. *Diamond Relat. Mater.* **2005**, *14*, 881−886.

(66) Roy, S. S.; Papakonstantinou, P.; Okpalugo, T. I. T.; Murphy, H. Temperature Dependent Evolution of the Local Electronic Structure of Atmospheric Plasma Treated Carbon Nanotubes: Near Edge X-Ray Absorption Fine Structure Study. *J. Appl. Phys.* **2006**, *100*, 053703.

(67) Kuznetsova, A.; Popova, I.; Yates, J. T.; Bronikowski, M. J.; Huffman, C. B.; Liu, J.; Smalley, R. E.; Hwu, H. H.; Chen, J. G. Oxygen-Containing Functional Groups on Single-Wall Carbon Nanotubes: NEXAFS and Vibrational Spectroscopic Studies. *J. Am. Chem. Soc.* **2001**, *123*, 10699−10704.

(68) Nyberg, M.; Hasselström, J.; Karis, O.; Wassdahl, N.; Weinelt, M.; Nilsson, A.; Pettersson, L. G. M. The Electronic Structure and Surface Chemistry of Glycine Adsorbed on Cu(110). *J. Chem. Phys.* **2000**, *112*, 5420−5427.

(69) Liu, L.; Chen, Y.; Xie, Y.; Tao, P.; Wang, Z.; Li, Q.; Wang, K.; Yan, C. Enhanced Interfacial Kinetics of Carbon Monolith Boosting Ultrafast Na-Storage. *Small* **2019**, *15*, 1804158.

(70) Hu, X.; Sun, X.; Yoo, S. J.; Evanko, B.; Fan, F.; Cai, S.; Zheng, C.; Hu, W.; Stucky, G. D. Nitrogen-Rich Hierarchically Porous Carbon as a High-Rate Anode Material with Ultra-Stable Cyclability and High Capacity for Capacitive Sodium-Ion Batteries. *Nano Energy* **2019**, *56*, 828−839.